

## Diagnosing and mitigating laser preheat induced mix in MagLIF

A. J. Harvey-Thompson,<sup>1</sup> M. R. Weis,<sup>1</sup> E. C. Harding,<sup>1</sup> M. Geissel,<sup>1</sup> D. J. Ampleford,<sup>1</sup> G. A. Chandler,<sup>1</sup> J. R. Fein,<sup>1</sup> M. E. Glinsky,<sup>1</sup> M. R. Gomez,<sup>1</sup> K. D. Hahn,<sup>1</sup> S. B. Hansen,<sup>1</sup> C. A. Jennings,<sup>1</sup> P. F. Knapp,<sup>1</sup> R. R. Paguio,<sup>2</sup> L. Perea,<sup>1</sup> K. J. Peterson,<sup>1</sup> J. L. Porter,<sup>1</sup> P. K. Rambo,<sup>1</sup> G. K. Robertson,<sup>1</sup> G. A. Rochau,<sup>1</sup> D. E. Ruiz,<sup>1</sup> J. Schwarz,<sup>1</sup> J. E. Shores,<sup>1</sup> D. B. Sinars,<sup>1</sup> S. A. Slutz,<sup>1</sup> G. E. Smith,<sup>2</sup> I. C. Smith,<sup>1</sup> C. S. Speas,<sup>1</sup> and K. Whittemore<sup>1</sup>

<sup>1</sup>Sandia National Laboratories, P.O. Box 5800, Albuquerque, New Mexico 87185, USA

<sup>2</sup>General Atomics, San Diego, California 92121, USA

(Received 3 August 2018; accepted 29 October 2018; published online 16 November 2018)

A series of Magnetized Liner Inertial Fusion (MagLIF) experiments have been conducted in order to investigate the mix introduced from various target surfaces during the laser preheat stage. The material mixing was measured spectroscopically for a variety of preheat protocols by employing mid-atomic number surface coatings applied to different regions of the MagLIF target. The data show that the material from the top cushion region of the target can be mixed into the fuel during preheat. For some preheat protocols, our experiments show that the laser-entrance-hole (LEH) foil used to contain the fuel can be transported into the fuel a significant fraction of the stagnation length and degrade the target performance. Preheat protocols using pulse shapes of a few-ns duration result in the observable LEH foil mix both with and without phase-plate beam smoothing. In order to reduce this material mixing, a new capability was developed to allow for a low energy ( $\sim 20$  J) laser pre-pulse to be delivered early in time ( $-20$  ns) before the main laser pulse ( $\sim 1.5$  kJ). In experiments, this preheat protocol showed no indications of the LEH foil mix. The experimental results are broadly in agreement with pre-shot two-dimensional HYDRA simulations that helped motivate the development of the early pre-pulse capability. *Published by AIP Publishing.*

<https://doi.org/10.1063/1.5050931>

### I. INTRODUCTION

The Magnetized Liner Inertial Fusion (MagLIF) scheme<sup>1</sup> is a novel magneto-inertial confinement fusion (ICF) concept that has demonstrated thermonuclear fusion yields on the Z Facility.<sup>2,3</sup> In MagLIF, a cylindrical liner is filled with D<sub>2</sub> fuel that is preheated ( $T_i = 100$ – $200$  eV) and pre-magnetized with an axial  $B_z = 10$ – $30$  T magnetic field before being imploded using the Z pulsed-power generator (up to 22 MA, 100 ns current rise time). With this approach, conditions for thermonuclear fusion can be reached with modest implosion velocities ( $\sim 100$  km/s), fuel convergence ratios (ratio of the initial to the final diameter of  $\sim 30$ – $40$ ), and pressures ( $\sim 1$  Gbar).

Fuel preheat is achieved using the Z-Beamlet laser<sup>4</sup> ( $2\omega$ , 527 nm, 1 TW, up to 4 kJ) that deposits energy into the fuel via inverse Bremsstrahlung absorption. Optimal laser preheat occurs when the liner first begins to implode, about  $\sim 60$  ns before peak neutron production. Applying preheat at this time maximizes the compressional heating of fuel and enables sufficient fuel temperatures to be achieved at stagnations with a relatively slow implosion, provided that sources of energy loss are controlled. The primary source of energy loss, electron thermal conduction, is reduced in the radial direction by the applied axial magnetic field. Radiative energy losses from the (initially pure) D<sub>2</sub> fuel can be important as well and can increase dramatically if higher atomic number (Z) contaminants are introduced, reducing the performance.

Two-dimensional (2D) LASNEX<sup>5</sup> and HYDRA<sup>6</sup> simulations have shown that the neutron yield is degraded by the quantity, species, and time at which the mix is introduced. The simulations show that there is a large sensitivity to all

three of these factors. Contaminants introduced early in time reduce the target performance most strongly since the relatively long implosion ( $\sim 60$  ns) gives ample time for radiative losses. Laser preheat has the potential to introduce the mix early in the implosion. The direct illumination of the laser-entrance-hole (LEH) foil, used to contain the fuel, can cause the foil material to be injected and mixed into the fuel. In addition, the ablation of inner target surfaces can occur after the interaction with the blast-wave generated in the heated fuel.

In this paper, we present the results of a series of MagLIF experiments that were conducted to investigate the material mix introduced from various target surfaces during the laser preheat stage. Material surfaces that could potentially introduce mix contaminants into the fuel were coated with mid-Z materials, specifically cobalt and manganese. At stagnation, the material from the coatings which is mixed with the fuel emits K shell x-rays that are observed with a time integrated, axially resolved spectrometer. The spectra effectively show the axial extent of the material from each coated surface at stagnation and therefore the axial extent of the mix from those surfaces. This technique is applied to different laser preheat protocols that vary the laser temporal pulse shape, spot size, beam conditioning, and gas fill density.

This paper is structured as follows: In Sec. II, the experimental setup is described including the coatings applied to MagLIF targets and the various preheat protocols used in the experiments. Section III describes the results from experiments, in particular where coatings that were applied to various components are observed at stagnation for different

preheat protocols. Section IV describes HYDRA simulations of the preheat protocols that show how differences in the LEH foil disassembly affect the amount of the foil material introduced into the target. Finally, Sec. V summarizes the results.

## II. EXPERIMENTAL SETUP

### A. MagLIF target design and coatings

The design of the MagLIF targets used in the experiments is shown in Fig. 1. The target design is very similar to those used in previous experiments. All experiments used liners with an aspect ratio (ratio of the outer radius to the wall thickness) of 6 with a 10-mm-long active imploding region. Before pressurization, the LEH foil is  $1.77\ \mu\text{m}$  thick, which is the minimum thickness required to hold the fuel gas pressure at the designed LEH window diameter (60 or 90 psi for 3 mm or 2 mm diameter windows, respectively). The top cushion region located below the LEH foil prevents the enhanced magneto-Rayleigh-Taylor (MRT) instability growth at the anode end of the liner during the implosion (a similar bottom cushion prevents the MRT growth at the cathode end). The top cushion provides a 1.5 mm axial offset between the LEH foil and the imploding portion of the target. All fuel-facing surfaces are Beryllium with the exception of the LEH foil, which is composed of polyimide and of the mid-Z coatings that were applied to investigate the material mix.

In order to determine whether laser preheat causes mixing of any target material with the fuel in the imploding region, mid-Z coatings were applied to various surfaces on the target. The coatings applied to the seven integrated MagLIF shots that are discussed in this paper are summarized in Fig. 2 and Table I. The shots focused on diagnosing what are hypothesized to be the most likely sources of the problematic mix introduced during preheat, specifically the LEH foil, top cushion, and bottom cushion. The LEH foil is thought to be most problematic because it interacts strongly with the laser during preheat, while its density remains high,

and it includes C, N, and O ions which radiate more than the Be of the other fuel-facing surfaces. The top cushion is also a potential source of the mix because the inner diameter (ID) of the top cushion (3 mm) is smaller than the imploding liner (4.65 mm), and it is positioned immediately below the LEH foil, where the strongest laser interaction takes place. Materials can be ablated from the top cushion either from direct laser illumination, interaction with the laser-produced blast wave in the fuel, or by radiation ablation from x-rays generated by the heated LEH foil material or gas fill plasma. Finally, the bottom cushion is also a potential source of the laser-induced mix because it is possible for the laser to strike the top surface of the cushion and the ablate material.

We chose Co and Mn coatings because they emit K shell radiation at photon energies greater than 6 keV that can be transmitted through the imploded liner [ $\rho R_{\text{liner}} \sim 0.8\ \text{g/cm}^2$  (Ref. 7)] and because the radiation emission only emits efficiently at fuel temperatures greater than 1.5 keV, close to peak burn. The emission is observed with the XRS3 diagnostic,<sup>8</sup> a time integrated, axially resolved spherical crystal spectrometer that was modified to observe the energy range  $h\nu \sim 6.3\text{--}8.1\ \text{keV}$  which encompasses the Co He- $\alpha$  and Ly- $\alpha$  lines (at 7.242 and 7.526 keV, respectively) and the Mn He- $\beta$  line at 7.267 keV. The spectrometer is sufficiently sensitive such that, provided that the material reaches the necessary temperature at stagnation, the K shell emission will be observed even for dopant quantities that are not expected to significantly degrade the yield if introduced at the time of preheat (as little as 0.0001%, or 1 ppm, Co mixed into the fuel). The spatial resolution of the spectrometer in the axial direction is  $200\ \mu\text{m}$ , allowing the axial extent of the coating materials to be determined with good precision along the  $\sim 10\ \text{mm}$  stagnation column. A dual spherical crystal imager setup that observes the Co He- $\alpha$  line and the nearby continuum region was also fielded on all shots described in this paper which shows essentially the same information but with higher spatial resolution. The crystal imager setup and processing will be part of a future paper that describes this diagnostic technique.

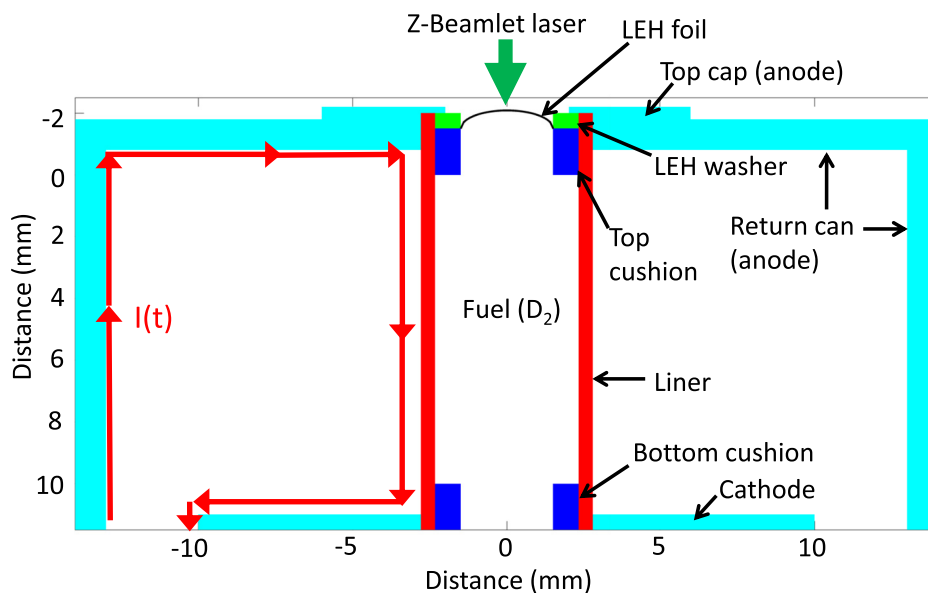


FIG. 1. Illustration of the general MagLIF target geometry used in all experiments and simulations reported in this paper.

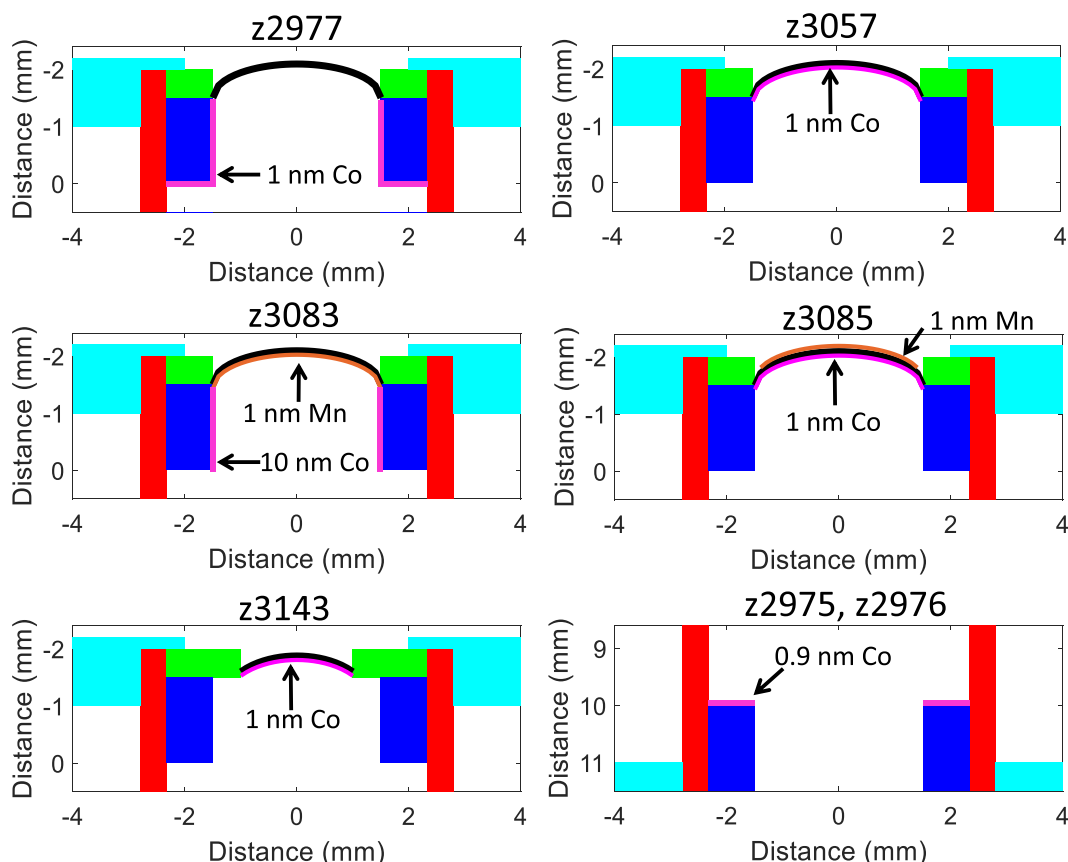


FIG. 2. Geometry of the anode (or cathode) region of the target for each experiment showing the locations of coatings applied.

Since we are using mid-Z coatings to assess material mixing, the material in the coatings might also degrade the target performance during the implosions. Figure 3 shows the results from multiple 1D LASNEX simulations of integrated MagLIF implosions.<sup>5</sup> Various amounts of different dopants were uniformly mixed into the fuel at the start of the simulation, and the neutron yield is calculated as a fraction of the clean yield (i.e., when no dopants are added). The simulations used a Direct Configuration Accounting (DCA) cooling model<sup>9</sup> which does not assume Local Thermodynamic Equilibrium and target parameters relevant to the MagLIF experiments described in this paper (10 T B field, 1.34 kJ preheat energy,

and similar time dependent drive current). The curves shown in Fig. 3 can be used to estimate the neutron yield degradation for the Co and Mn coatings described in this paper. In simulations, the amount of material required to produce a given degradation scales approximately as  $Z^3$ ,<sup>5</sup> and the difference between the behavior of Fe, Co and Mn is relatively small ( $\leq 20\%$  difference in the number of atoms required to produce a similar degradation). For the purposes of this paper, therefore, the Co and Mn coatings are assumed to behave similar to Fe in Fig. 3.

The amount of the mix introduced by a 1 nm thick Co coating on a 3 mm diameter LEH foil ( $\sim 8.6 \times 10^{13}$  Co atoms)

TABLE I. Summary of the target configurations and stagnation parameters for the shots described in this paper. For each experiment, the laser energy incident on the target is split into the pre-pulse and main pulse energies, respectively, except for z3143 which lists the pre-pulse, foot pulse, and main pulse energies, respectively.

Shot no.	Z2975	Z2976	z2977	Z3085	Z3057	Z3083	Z3143
Preheat protocol	No-DPP	No-DPP	No-DPP	No-DPP	With-DPP	With-DPP	Co-injection
Laser energy (J)	371 + 2026	357 + 1881	318 + 1714	324 + 1632	103 + 1283	80 + 1380	24 + 183 + 1626
Fuel density (mg/cc)	0.7	0.7	0.7	0.7	0.7	0.7	1.05
DD yield	$4.5 \times 10^{11} \pm 20\%$	$8.0 \times 10^{11} \pm 20\%$	$3.0 \times 10^{12} \pm 20\%$	$4.2 \times 10^{11} \pm 20\%$	$2.0 \times 10^{12} \pm 20\%$	$7.0 \times 10^{11} \pm 20\%$	$2.2 \times 10^{11} \pm 20\%$
Tion (keV)	$1.6 \pm 20\%$	$1.6 \pm 20\%$	$2.5 \pm 20\%$	$1.8 \pm 20\%$	$2.4 \pm 20\%$	$1.8 \pm 20\%$	$2.1 \pm 20\%$
Notes	0.9-nm-thick Co on bottom cushion	0.9-nm-thick Co on bottom cushion	1-nm-thick Co on top cushion	1-nm-thick Co coating on LEH	1-nm-thick Co on LEH	10-nm-thick Co coating on top cushion, 1 nm thick Mn coating on LEH	1-nm-thick Co coating on LEH. 3 ppm Kr dopant in fuel

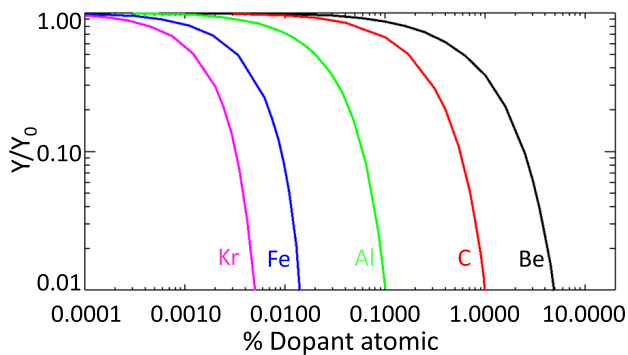


FIG. 3. Results from 1D LASNEX simulations of integrated MagLIF implosions in which a fraction of various dopants have been added to the fuel at the start of the simulation. The neutron yield ( $Y$ ) is normalized to the clean yield ( $Y_0$ , pure  $D_2$  fuel).

is insufficient to significantly reduce the neutron yield or stagnation temperature even if all the Co atoms were volumetrically mixed with the deuterium atoms in the imploding region ( $\sim 1.8 \times 10^{19}$  D atoms in a 10 mm tall region at 0.7 mg/cc) at the time of preheat. The resulting mix fraction of 0.00048% would reduce the yield by less than 10%. Regarding the top cushion, if all the material in the 1 nm and 10 nm Co coatings was mixed into the fuel, this would equate to Co mix fractions of 0.0075% and 0.075%, respectively, which would reduce the yield by factors of  $\sim 10$  and  $>100$ , respectively, if mixed volumetrically at the time of preheat. Finally, the 0.9 nm Co coatings on the bottom cushions would introduce up to 0.0021% mix into the fuel, sufficient to reduce the yield by  $\sim 30\%$ .

## B. Design of preheat protocols

The preheat protocols used in MagLIF were developed with focused experiments guided by numerical simulations. The primary design tool used is the radiation-hydrodynamics code HYDRA, which will be discussed in Sec. IV. Prior to their use in integrated MagLIF experiments on the Z-machine, each preheat protocol is tested in laser-gas-cell experiments at a dedicated test facility (the Pecos target chamber) where diagnostics are available to measure the energy absorbed in the gas and observe backscattered light produced by laser plasma instabilities (LPI).<sup>10,11</sup> The development of the preheat protocols will be discussed in more detail in a future paper. The focus of this paper is to assess the material mixing introduced into the fuel by each preheat protocol.

As shown in Fig. 4 and summarized in Table I, three different preheat protocols were tested across the seven shots described in this paper. With these protocols, we varied the laser temporal pulse shape, spot size, amount of beam conditioning, and gas fill density. These changes led to significantly different powers and intensities at the LEH foil, the energy deposited into the fuel, the amount of LPI produced during preheat, and the amount of LEH foil material pushed into the fuel.

In shots z2975, z2976, z2977, and z3085, a similar preheat protocol was used as in integrated MagLIF experiments reported previously,<sup>3</sup> termed the “no-DPP” protocol in this paper. In this protocol, the Z-beamlet (ZBL) laser has no smoothing techniques applied. Instead, the focal spot is

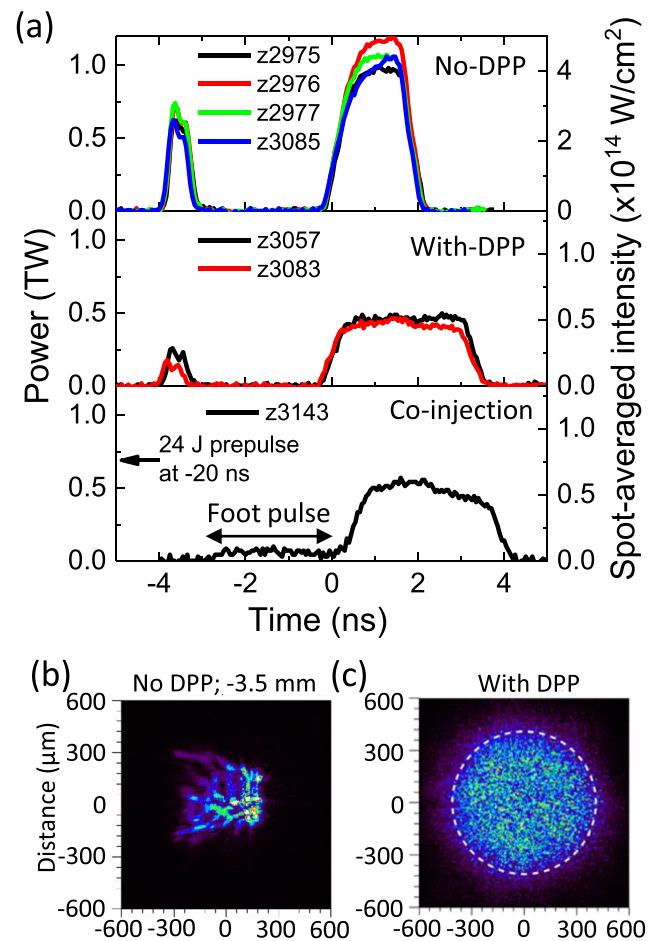


FIG. 4. (a) Laser pulse shapes for the preheat protocols tested. The spot-averaged intensities assume uniform illumination within the spatial envelopes described. The vertical scale is different for the co-injection pulse shape, so the foot pulse can be clearly seen. The spatial profiles of the laser spot when no distributed phase plate (DPP) smoothing is applied (b) and with an 1100  $\mu\text{m}$  distributed phase plate (DPP) (c) are also shown.

positioned  $\sim 3.5$  mm above the surface of the LEH foil so that the beam defocuses to produce an  $\sim 500$ - $\mu\text{m}$  square spot on the top of the LEH foil. In this case, the intensity profile of the spot is very irregular with significant peak-to-valley variations, as shown in Fig. 4(b) and as discussed in detail in the study by Geissel *et al.*<sup>11</sup> The spot-averaged intensity ( $\sim 4 \times 10^{14}$  W/cm<sup>2</sup>) is such that significant LPI including stimulated Brillouin scattering (SBS) and filamentation would be expected to occur during preheat. The pulse shape is split into a 0.5 ns long,  $\sim 350$  J pre-pulse that arrives at the LEH window 3.5 ns before a 2 ns long, 2 kJ main pulse. The purpose of the pre-pulse is to pre-expand the LEH foil material so that it becomes underdense by the time the main pulse arrives. While the design of the preheat protocol was guided by simulations, the irregular spot profile makes realistic simulations of the behavior of the preheat protocol extremely challenging. Furthermore, significant levels of LPI are generated with this protocol. Since LPI is not modeled in our HYDRA simulations, poor agreement is obtained with experiments. Thus, detailed predictions are not presented here for this protocol.

Shots z3057 and z3083 used a “with-DPP” preheat protocol, so-called because a distributed phase plate (DPP) optic

was used to produce a reproducible 1100- $\mu\text{m}$  diameter spot (containing 95% of the energy) with an 8th order super-Gaussian irradiance profile ( $I(r) \propto \exp[-2(\frac{r}{a})^8]$ ) at the best focus which was positioned at the LEH foil.<sup>11</sup> As shown in Fig. 4, applying DPP smoothing results in a broadly smoother profile that contains a high-frequency speckle pattern and reduces the on-target peak and spot-averaged intensities for the same temporal laser pulse which, in offline experiments, dramatically reduces the LPI observed.<sup>10,11</sup> The low levels of LPI and the well-understood, reproducible spot profile mean that the with-DPP preheat protocol can be modeled more accurately and so produce a more predictable energy deposition profile in the fuel. As with the no-DPP protocol, the with-DPP protocol has a pre-pulse 3.5 ns before the main pulse that contains  $\sim 80$  J to reduce the LEH foil density. The design of the pre-pulse was guided by HYDRA simulations, described in Sec. IV, to minimize the kinetic energy associated with LEH foil particles moving downwards into the imploding region while still allowing the main pulse energy to propagate into the gas.

The results presented in Sec. III A of this paper suggest that the with-DPP preheat protocol introduces the LEH foil mix into the imploding region of the target. This led to the development, guided by simulations discussed in Sec. IV, of the ‘‘co-injection’’ protocol used in z3143 which was designed to reduce the amount of LEH foil material mixed into the fuel. The delay time between the pre-pulse and the main pulse for the no-DPP and with-DPP protocols, limited by the maximum pulse length achievable by ZBL alone ( $\sim 6$ – $7$  ns), was insufficient for the LEH foil to fully rarify below the critical density before the main pulse arrived. To overcome this limitation, the co-injection protocol used the Z-Petawatt laser to deliver a low energy (24 J, 2 ns long), early (20 ns before the main pulse) pre-pulse that was injected along the same beam path as ZBL to pre-heat and expand the LEH foil. The ZBL laser then delivers the main pulse which has a 3-ns-long,  $\sim 0.06$  TW foot, intended to heat the expanded foil material (discussed more in Sec. IV), followed by a 3-ns-long,  $\sim 0.55$  TW main pulse. The co-injection protocol applied the same 1.1 mm DPP smoothing used in the with-DPP protocol.

For the experiments discussed, the fuel density and LEH foil parameters are also considered part of the preheat protocols. For the no-DPP and with-DPP preheat protocols, the fuel density was 0.7 mg/cc ( $n_e/n_c \sim 0.05$ ), the LEH foil thickness was 1.77  $\mu\text{m}$ , and the LEH diameter was 3 mm. For the co-injection preheat protocol, the fuel density was 1.05 mg/cc ( $n_e/n_c \sim 0.075$ ), the LEH foil thickness was 1.77  $\mu\text{m}$ , and the LEH diameter was reduced to 2 mm to allow the LEH foil to withstand the higher fuel pressure. The increased fuel density for the co-injection protocol was intended to reduce the inverse bremsstrahlung absorption length of the fuel, which allowed more preheat energy to be coupled into the imploding region of the target. Simulations also suggest that increasing the fuel density in integrated experiments may modestly reduce the convergence ratio when the peak neutron production occurs<sup>5,12</sup> but requires more coupled preheat energy to obtain the equivalent target performance.

### III. RESULTS

A summary of the target configurations and stagnation parameters (neutron yield and neutron-averaged ion temperature) for the shots described is given in Table I. The neutron yields are determined from several neutron-activation detectors.<sup>13</sup> The neutron spectra and the burn-weighted ion temperature are inferred from neutron time-of-flight detectors.<sup>14</sup> The neutron yields and ion temperatures are similar to those reported in previous experiments<sup>2,3</sup> where no coatings or dopants were used.

#### A. LEH foil coatings

As described in Sec. II A, the K-shell emission from the Co and Mn coatings was observed with a time-integrated, axially resolved spectrometer (the XRS3 diagnostic). An example XRS3 spectrum from shot z3057, which used the with-DPP preheat protocol, is shown in Fig. 5. Multiple emission lines are seen in the spectrum including He-like and fluorescence emission from Fe<sup>7</sup> and Ni trace impurities in the Be liner, which are believed to mix into relatively cool outer fuel layers late in the implosion. The emission from these lines extends the whole length of the imploding region of the target from the anode-side (at 0 mm) to the cathode-side (at 10 mm). The 1-nm Co dopant placed on the underside of the LEH foil in z3057 emits both He-like and H-like lines at stagnation, extending from the top of the target to  $\sim 6$  mm into the 10-mm-long imploding region. The Co emission suggests that the LEH foil material is mixed into the hot fuel core over this axial range. Since Co is applied as a coating to the LEH foil, the amount of the foil material is not necessarily related to the amount of Co emission observed. Significant changes in continuum and line emission are observed over the axial extent of the spectrum. This is due to several factors that may vary significantly along the length of the stagnation column such as the liner  $\rho R$ , the fuel temperature and density, and the amount of the mix introduced into the fuel. Separating these various contributions is challenging and requires a more sophisticated analysis of the spectrum and other diagnostics than is presented here.

A comparison of the Co emission from shots with three different preheat protocols: z3057 (with DPP), z3085 (no DPP), and z3143 (co-injection), is shown in Fig. 6. Compared to z3057, shot z3085 has weaker Co He- $\alpha$  and satellite lines and the spatial extent of the emission is smaller, extending only  $\sim 2.5$  mm into the imploding region. The crystal used in z3085 had a factor 3 lower reflectivity than in shots z3057 or z3143, which is compensated for in the processing. The data suggest that the no-DPP protocol does not push the LEH foil material as far into the target compared to the with-DPP preheat protocol. The 1 nm Mn coating placed on top of the window in z3085 did not produce the observable He- $\beta$  line emission ( $h\nu = 7.267$  keV) in the spectrum, indicating that either the material from the top surface of the LEH foil does not mix into the fuel or the amount of coating mixed in is not sufficient to produce an observable signal.

In z3143, no Co emission is observed, indicating that very little LEH material is injected into the fuel by the co-injection preheat protocol. The difference between the

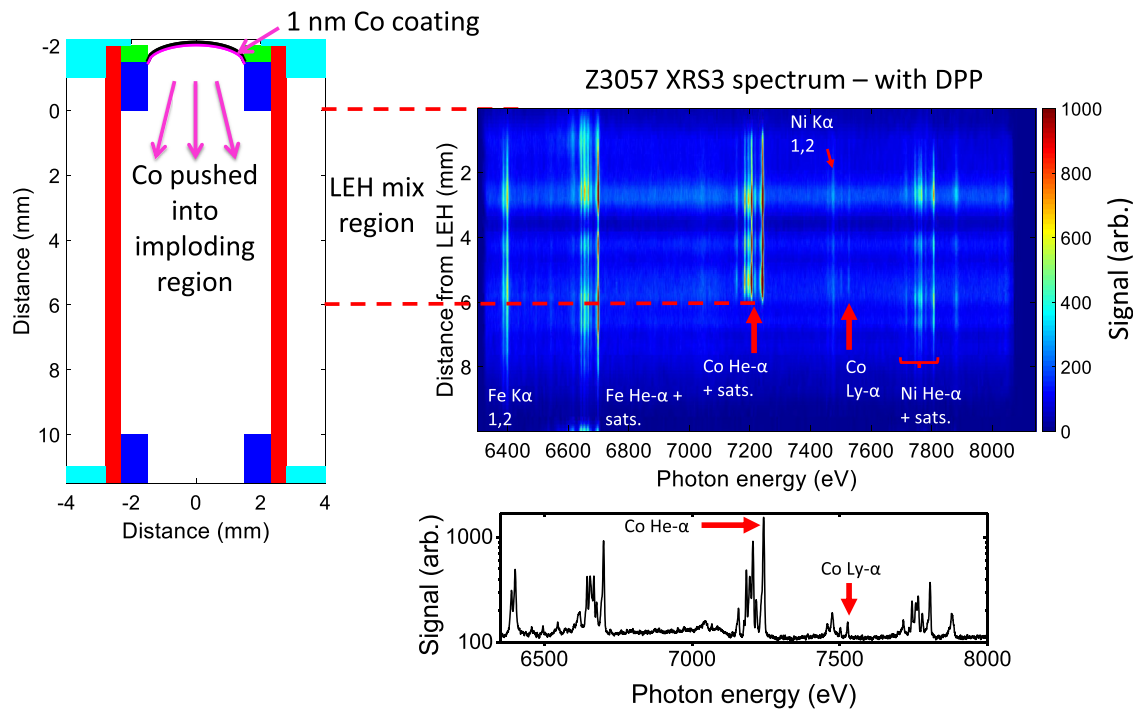


FIG. 5. A diagram of the target in z3057 and the full XRS3 spectrum recorded in that shot. The axial height of XRS3 is registered such that the top of the spectrum aligns with the top of the imploding region in the target drawing. The Co K shell lines can be seen extending  $\sim 6$  mm into the imploding region of the target down from the anode side. This implies mixing from the LEH window material to the target fuel. A lineout of the spectrum is shown averaged between 1 and 5.3 mm into the target.

data in z3057 and z3143 is dramatic. This result suggests that (1) the laser can push the window material into the fuel and (2) this effect can be controlled by appropriately tailoring the laser's temporal pulse shape.

While it is possible to further characterize the plasma conditions with a more detailed analysis of the spectra collected in these experiments,<sup>15,16</sup> this is not pursued here and will be the subject of a future paper.

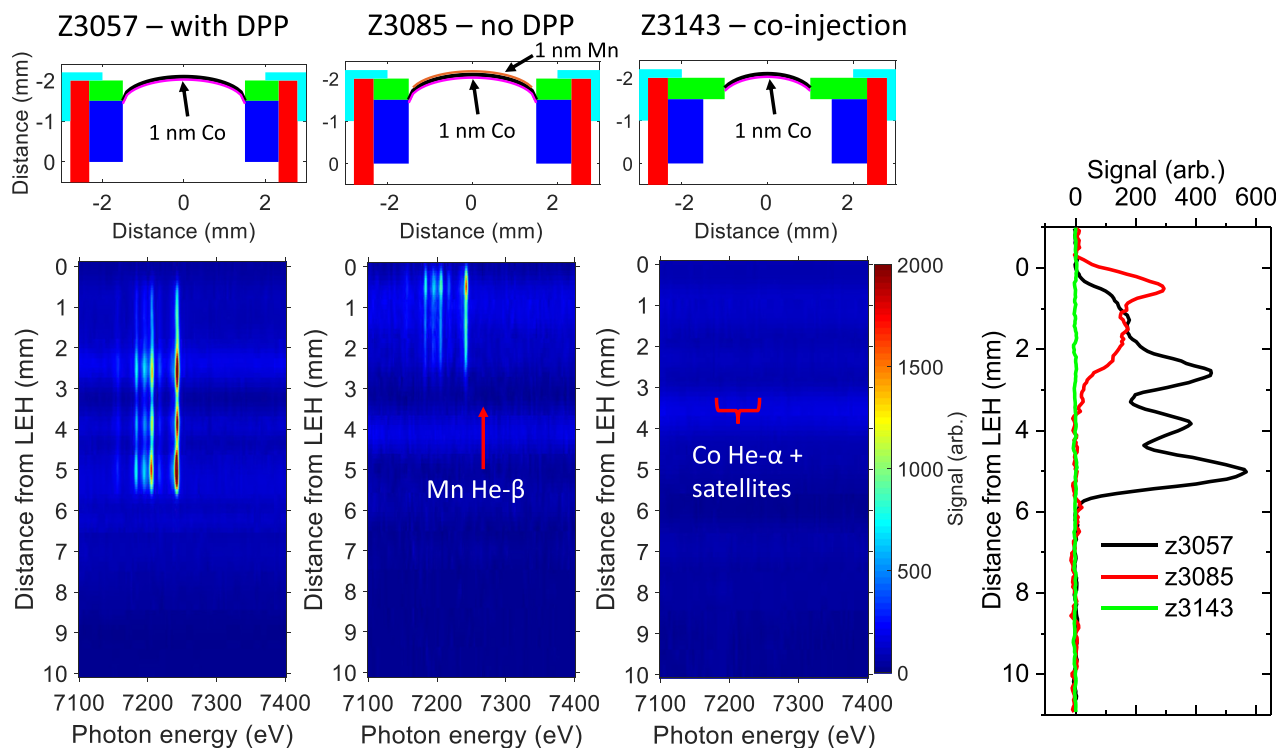


FIG. 6. XRS3 spectra recorded in three shots that used a 1 nm Co coating on the fuel-facing side of the LEH foil. The spectra are registered such that the top is aligned with the top (anode side) of the imploding region. Shot z3085 also had a 1 nm Mn coating on the top surface of the foil from which the He- $\beta$  line emission ( $h\nu = 7.267$  keV) would be observable in the spectrum shown but is not seen. The right hand plot shows vertical lineouts of the Co He- $\alpha$  line (averaged between 7220 and 7250 eV) with the continuum emission (averaged between 7250 and 7280 eV) subtracted.

## B. Top and bottom cushion coatings

As described in Sec. II, z2977 used a 1-nm Co coating on the fuel-facing surface of the top cushion and the no-DPP preheat protocol. The XRS3 spectrum from this experiment is shown in Fig. 7(a). The Co He- $\alpha$  line is observed only very weakly  $\sim 10$  counts/pixel above the background compared to hundreds for z3057 and z3085 between  $\sim 2$  and 4 mm into the imploding region, as shown in Fig. 7(b), with no Co emission observed above that. Because the Co emission only appears at the location where the continuum emission is the brightest, it is possible that Co elsewhere in the pinch would not emit brightly enough to be observed. As discussed in Sec. III A, there are many factors that contribute to the intensity of the observed emission, including the increased mix in this region although that cannot be concluded based on these data alone.

The neutron yield measured in z2977 ( $3.0 \times 10^{12} \pm 20\%$ ) is nominally equivalent to the highest neutron yield measured using the no-DPP preheat protocol without a Co coating (z2839— $3.2 \times 10^{12} \pm 20\%$ ). However, in spite of this, the mix from the top cushion cannot be definitively ruled out. For

example, if the Co coating in z2977 were responsible for a 10% decrease in yield (within the uncertainty of our measurements), this would imply a volumetric Co mix fraction of 0.0007%. As described in Sec. II, mixing all Co from the 1 nm top cushion coating into the imploding region of the fuel would introduce an atomic mix fraction of 0.0075%, degrading the yield by a factor 10. Therefore, a 10% degradation in yield would be consistent with only  $\sim 9\%$  of the Co coating being uniformly mixed into the imploding region of the fuel.

Since Co is applied as a coating in z2977, it is possible for substantially more Be than Co to have been ablated from the top cushion if a deep enough layer of the material had been ablated. However, the performance degradation is much less sensitive to mix from Be than the higher Z Co by the atomic fraction. For example, the atomic mix fraction of Be required to reduce the neutron yield by 50% is  $\sim 0.6\%$ . This is  $\sim 1000$  times less than the Co mix fraction required for a 10% yield degradation. To produce this ratio of Co to Be atoms, in locations where the top cushion material has been ablated, the minimum average ablation depth would need to be  $\sim 0.7 \mu\text{m}$  (or 730 times the thickness of the Co coating) as illustrated in Fig. 8, and the material would need

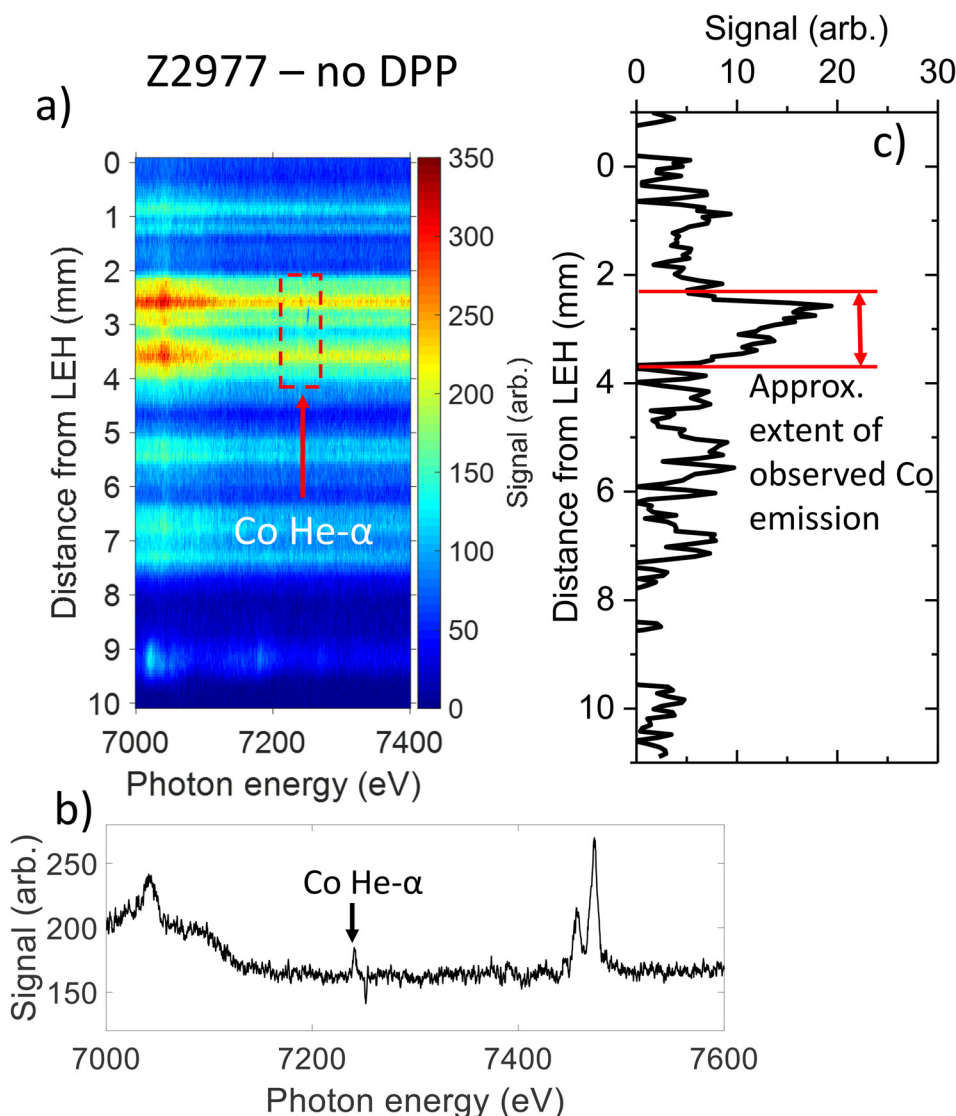


FIG. 7. The XRS3 spectrum recorded in z2977 (a) showing the region where the Co He- $\alpha$  line is observed, (b) a spectral lineout of the XRS3 data averaged between 2 and 3.5 mm into the imploding region, and (c) an axial lineout of the Co He- $\alpha$  line (averaged between 7237.6 and 7245.05 eV) with the continuum emission (averaged between 7250 and 7280 eV) subtracted.

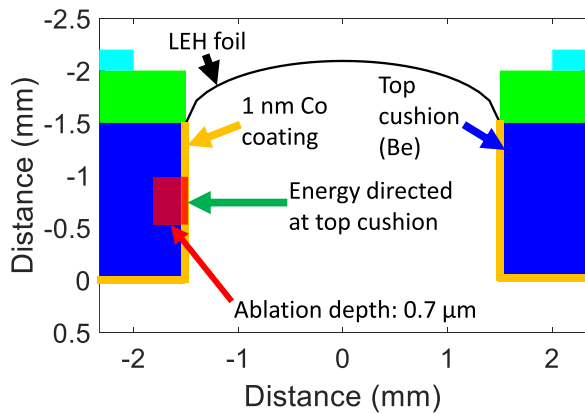


FIG. 8. A diagram of the top cushion region of the target used in z2977, illustrating how localized ablation of the top cushion could mix in sufficient Be to degrade the yield by 50%.

to be transported with Co into the imploding region of the fuel. These results alone cannot rule out this scenario.

Shot z3083 also investigated top cushion mix but using the with-DPP preheat protocol. Since the Co emission from a 1 nm top cushion coating was relatively weak in z2977, z3083 used a 10 nm Co coating on the fuel-facing surface of the top cushion. A 1 nm Mn coating was also applied to the fuel-facing surface of the LEH foil, so the relative location of LEH foil and top cushion material could be investigated simultaneously. The XRS3 spectrum from this experiment is shown in Fig. 9. The Mn He- $\beta$  line at 7.267 keV is observed extending  $\sim 4.5$  mm down from the top of the target, a similar distance to the Co emission lines in shot z3057 which used the same preheat protocol. In z3083, the Co emission lines are observed only between 4 and 6 mm into the target, indicating that the material from the top cushion is present

between these axial locations at stagnation. Interestingly, the top of the Co emission coincides with the bottom of the Mn emission. A possible interpretation is that the top cushion material is being pushed down into the target along with the D<sub>2</sub> fuel by the bulk downwards motion of the LEH foil material. Note that this is not observed in radiation-hydrodynamic simulations, which do not show the top cushion material entering the imploding region and likely do not capture the liberation of the material mix from the top cushion accurately. The result is somewhat surprising because it suggests that the materials remain relatively discrete not only during laser preheat, when the mix material is assumed to be first generated by the laser, but also throughout the entire implosion. The same process may also explain why the top cushion material is only observed between 2 and 3.5 mm into the target for the no-DPP protocol in z2977. This depth is consistent with the observation of the LEH foil material extending 2 mm into the target in z3085. It is also possible that the Co coating does not represent the full extent of the top cushion mix.

Shot z3083 returned a reasonably high neutron yield of  $7.0 \times 10^{11} \pm 20\%$ . Again, an estimate of the amount of the Co mix can be calculated by comparing the yield in z3083 to the best performing shot using the with-DPP preheat protocol (z3040— $4.1 \times 10^{12} \pm 20\%$  neutrons). In this case, the approximate factor of 6 decrease in yield between z3040 and z3083 is outside the error bars of the measurement and, if it is attributed to the Co coating alone, would require an atomic Co mix fraction of 0.007%. The amount of Co present in the coating would produce 0.075% atomic mix if all the Co was mixed into the fuel contained within the imploding region at the time of preheat, and  $\sim 11$  times more than is required to reduce the yield by a factor of 6. As in z2977, there is a

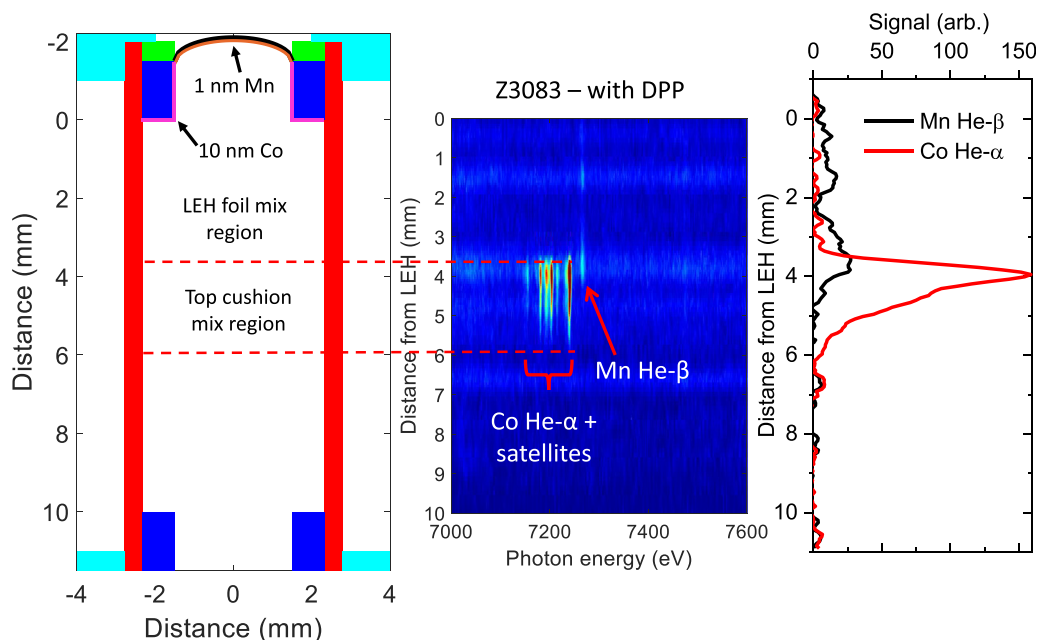


FIG. 9. A diagram of the target used in z3083 and the XRS3 spectrum recorded in that shot. The right hand plot shows vertical lineouts of the Co He- $\alpha$  line (averaged between 7220 and 7250 eV) and the Mn He- $\beta$  line (averaged between 7260 and 7280 eV) with the continuum emission (averaged between 7280 and 7310 eV) subtracted. The Mn He- $\beta$  line extends  $\sim 4.5$  mm into the imploding region of the target. The Co He- $\alpha$  and satellite lines are observed only below  $\sim 3.5$  mm. This indicates that the LEH foil material and the top cushion material are present in mostly different regions of the stagnation.

possible scenario whereby sufficient Be could be mixed into the imploding region of the fuel from the top cushion to degrade the yield in this experiment by a factor 2. Assuming that the Co coating was responsible for a factor of 6 degradation in yield, approximately 120 times the number of Be atoms as Co atoms would be required to reduce the neutron yield by 50%. To produce this ratio of Co to Be atoms, the minimum average ablation depth would need to be 90 times that of the Co coating thickness, or  $0.9\ \mu\text{m}$ , and that material would need to be transported into the imploding region.

Because the bottom cushion surface is at risk of being directly illuminated by laser light, the mix from the bottom cushion is likely to be very dependent on the preheat protocol used. Both shots z2975 and z2976 used 0.9-nm-thick Co coatings on the top surface of the bottom cushions and the no-DPP preheat protocol. The XRS3 did not return usable data on one of the shots, and Co emission was not observed in the other. In these experiments, the neutron yields were  $\sim 4\text{--}7\times$  lower than the best shots that use the no-DPP preheat protocol. It is unlikely that the Co mix sufficient to reduce yields by this fraction would not have been observed on XRS3, which can detect as little as 1 ppm Co even at temperatures near 1.5 keV.<sup>17</sup> The low performance of these shots can thus not be definitively linked to the presence of the Co coating and is currently not understood. The results of these experiments therefore do not resolve whether the Be mix from the bottom cushion is significant for the no-DPP preheat protocol.

#### IV. HYDRA SIMULATIONS OF THE LEH FOIL MIX

As discussed in Sec. II B, the development of the preheat protocols was guided by 2D axisymmetric radiation-magneto-hydrodynamic simulations using the code HYDRA.<sup>18</sup> The laser absorption model in HYDRA accounts for inverse bremsstrahlung absorption and refraction but not LPI processes such as stimulated Raman scattering, SBS, and non-thermal filamentation. HYDRA has previously been used to successfully model MagLIF-relevant laser absorption experiments<sup>19</sup> and integrated MagLIF experiments.<sup>6</sup> HYDRA models the complete preheat stage, including the interaction with the LEH foil, and the transport of the LEH foil mix. The mix from other surfaces, such as the top and bottom cushions, has also been modeled with higher resolution simulations,<sup>6</sup> but at these conditions, the ablation of the material from these surfaces is predicted to be significantly less important than the LEH foil, and thus, it will not be discussed further. The simulations presented are of integrated MagLIF experiments, using the target geometry shown in Fig. 1, magnetized with 10 T, and include both laser preheat and the target implosion. These simulations used experimentally measured temporal profiles from Z experiments. For the with-DPP protocol, the z3040 laser-pulse shape was used, which contained within 10% of the energy of the z3057 and z3083 power pulses. This difference in the energy does not significantly change the amount of the mix introduced in the code and does not impact the conclusions in this paper. For the co-injection protocol, the measured power pulse from z3143 was used (see Fig. 4).

Lineouts of the density and temperature distributions present just before the start of the main pulse in simulations of the with-DPP and co-injection protocols are shown in Fig. 10 with the laser entering from the left. The dashed curves are window cells, and the solid curves represent deuterium cells. For the with-DPP protocol, simulations suggest that the foil material is still present at high densities ( $n_e \sim 2 \times 10^{21}\ \text{cm}^{-3}$  and  $n_e/n_c \sim 0.5$ ) and at low temperatures ( $T_e < 100\ \text{eV}$ ) by the time the main pulse arrives. Additionally, a shock is driven in the deuterium by the 100 J pre-pulse. This material will initially interact strongly with the main pulse until it is heated and expands. For the co-injection protocol however, the foil material density is reduced by the time the foot pulse arrives and is reduced further by the time the power increases in the main pulse. The main action of the foot pulse is to dramatically increase the temperature of the foil material so that it is both hot and underdense when the main pulse arrives.

The difference in pulse shapes and density distributions for the two preheat protocols results in a different pressure balance between the LEH foil material and the deuterium fuel after the main pulse turns off as shown in Fig. 11. For the with-DPP protocol, the foil material has a higher pressure than the fuel immediately below it, so the foil material should continue propagating into the fuel. For the co-injection protocol, however, the pressure between the fuel and the foil material is roughly equal. This allows the fuel pressure to arrest the downward (laser-propagation direction) motion of the foil more quickly.

Figure 12 shows the total kinetic energy associated with downwards (and upwards) moving LEH foil particles for the with-DPP and co-injection configurations as a function of time up until peak burn occurs in the simulation. This is

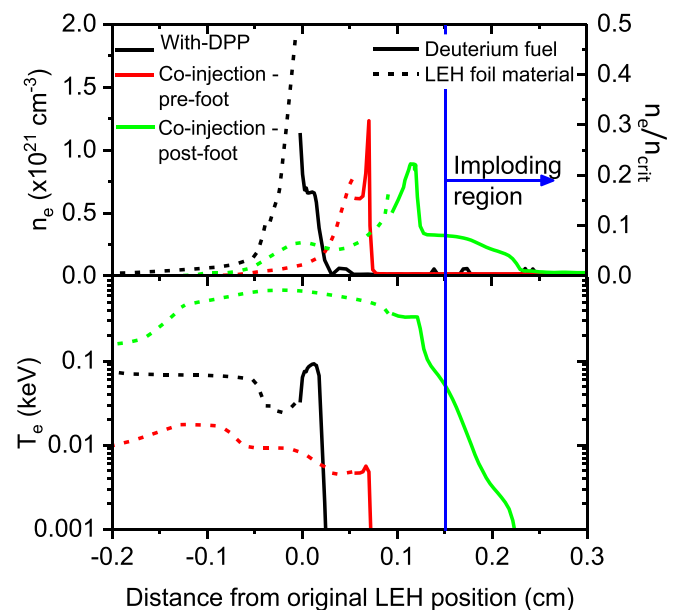


FIG. 10. Electron density and temperature distributions calculated from HYDRA simulations for the LEH foil material and deuterium fuel for the with-DPP and co-injection protocols. The plots for the with-DPP protocol are taken just before the main pulse starts, while for the co-injection protocol, the plots are taken just before the foot pulse and just before the main pulse starts. The laser enters from the left.

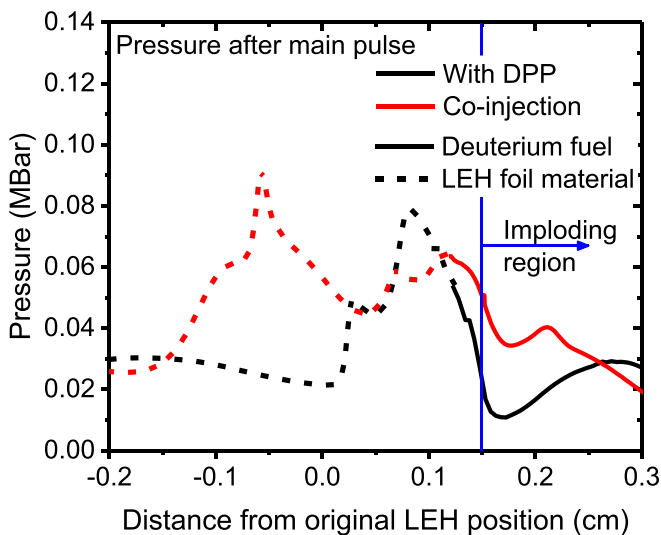


FIG. 11. Plot of the plasma pressure distribution for the LEH foil material and deuterium fuel for the with-DPP and co-injection protocols taken from HYDRA simulations immediately after the end of the main pulse. The laser enters from the left.

calculated by summing up the kinetic energy of only the downwards (or upwards) moving LEH foil material located below the initial location of the LEH foil to illustrate at what times and by what processes the LEH foil material is pushed into the imploding region of the target. For the with-DPP configuration, the downward kinetic energy in the foil material peaks at the end of the main laser pulse and then drops rapidly as the material begins to cool. Then, the pressure of

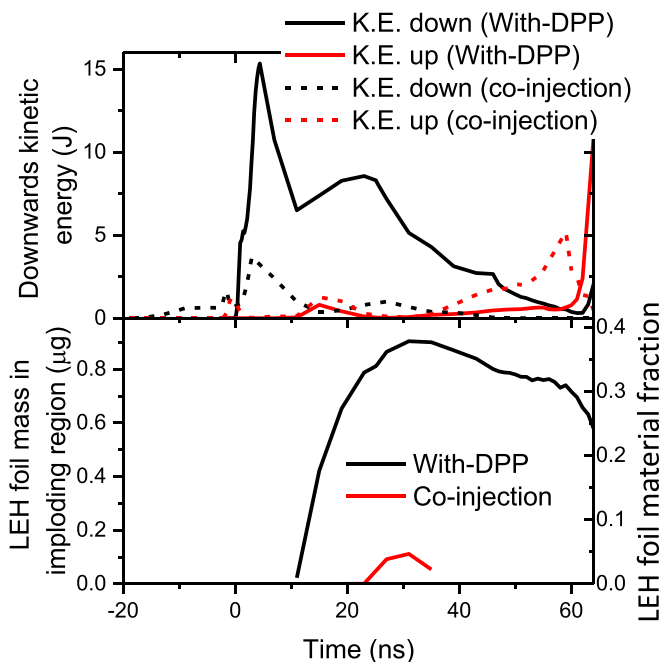


FIG. 12. Total downwards and upwards kinetic energy of the LEH foil material (top) and foil mass in the imploding region (bottom) as a function of time in simulations for the with-DPP and co-injection protocols. The main pulse of the laser starts at  $t = 0$  ns, and the peak neutron burn time is  $\sim 65$  ns for both configurations. The bottom plot also shows the amount of the foil material in the imploding region as a fraction of the amount of the foil material that the 1.1 mm diameter laser spot interacts with.

the  $D_2$  plasma immediately below the foil material slows the downwards motion. Also plotted in Fig. 12 is the LEH foil mass present in the imploding region of the simulations as a function of time. Because there is a 1.5 mm offset between the LEH foil and the imploding region, the LEH material only begins to enter the imploding region 10 ns after the main pulse starts. Around this time, the blast wave produced during preheat has reflected from the liner walls and propagates towards the axis where the foil material is present. Because more preheat energy is deposited near the top of the target, the reflected blast wave reaches the axis near the top of the target first before “zippering” down the axis. This imparts more downwards than upwards kinetic energy to the foil material and drags more foil material into the imploding region. The total mass of the foil material in the imploding region peaks at  $0.9 \mu\text{g}$ ,  $\sim 30$  ns after preheat, and then declines slightly as the fuel mass is lost out of both ends of the target during the implosion.

The co-injection protocol imparts downwards kinetic energy to the LEH foil material earlier in time and follows a similar behavior as the with-DPP protocol after the start of the main pulse. However, the magnitude of the downwards kinetic energy is substantially less than for the with-DPP protocol during and after the main pulse. This is because the early co-injection pulse pre-expands the foil, and then, later pulses do substantially less PdV work on the material. This results in substantially less foil material entering the imploding region of the target which peaks at  $\sim 0.1 \mu\text{g}$ . This material is effectively ejected during the implosion as the fuel mass is lost out the ends of the target.

Figure 13 shows an image of the fuel conditions in the simulation 4 ns before peak neutron production ( $\sim 62$  ns after the laser turns off; fuel convergence ratio,  $\sim 11$ ) along with the location of the LEH foil material for the with-DPP and co-injection protocols. In the simulation of the with-DPP protocol, the foil material extends virtually the entire length of the imploding region. The fuel pressure during the implosion has compressed a discrete column of the foil material onto the axis of the simulation for the duration of the implosion. This is potentially a symptom of the 2D symmetry, but it may also be a result of the lack of grid resolution or sub-grid turbulent mixing models. For the with-DPP protocol at 62 ns after laser preheat, the total amount of the LEH foil material present in the imploding column is  $0.66 \mu\text{g}$  compared to  $86.4 \mu\text{g}$  of deuterium. This is  $\sim 28\%$  of the polyimide mass that the 1.1 mm diameter laser spot illuminates directly. The amount of carbon-like (C, N, and O) atoms from the LEH present is  $\sim 0.1\%$  of the D atoms in the imploding region of the fuel at this time. If the carbon-like atoms were volumetrically mixed at the time of preheat, the yield would be expected to have degraded by 20% based on the curves in Fig. 3. However, in the simulations, the foil material mixes in after preheat as shown in Fig. 12 and is contained on the axis as shown in Fig. 13, both of which reduce the amount of degradation. In particular, a clean boundary (mix boundary line in Fig. 13) is maintained between the LEH foil material and the deuterium fuel which is likely unrealistic. The foil material being discretely located on the axis and not thoroughly atomically mixed

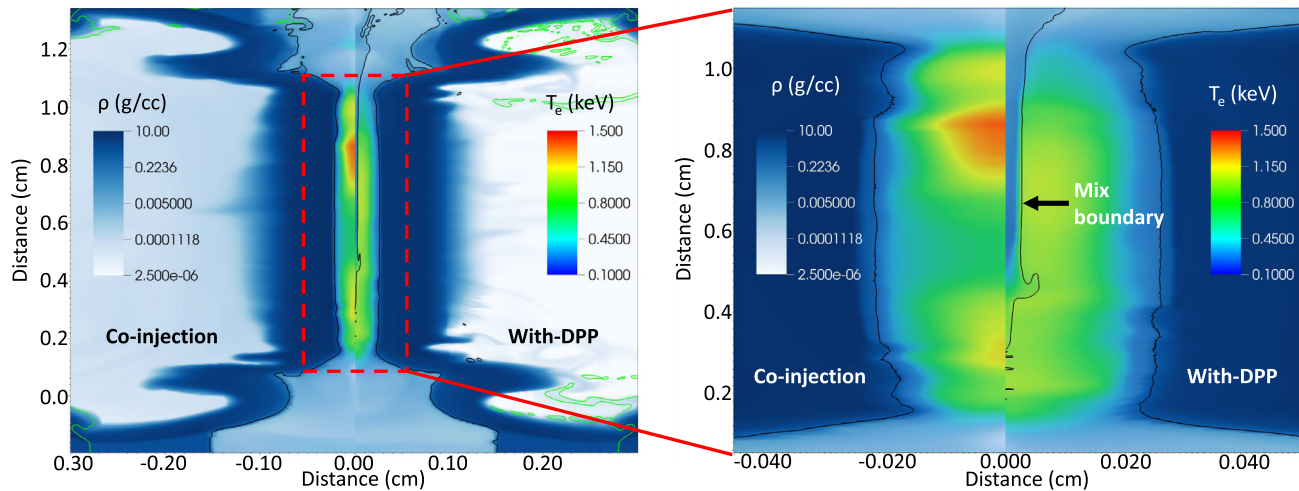


FIG. 13. Images of integrated MagLIF simulations taken at a fuel convergence ratio of  $\sim 11$ . The image on the right shows a zoomed-in view of the region enclosed in the red box shown in the image on the left. For each image, the left-hand side shows the results of the co-injection protocol and the right-hand side shows the results of the with-DPP protocol. The black line close to the axis marks the boundary where the LEH foil mix is present in the fuel. The LEH foil material extends almost the entire length of the fuel in the with-DPP case, whereas almost no foil material is present for the co-injection case.

with the fuel slows the transport of energy from the fuel because the surface area of the foil material region is low, and the radial thermal transport transverse is significantly reduced as a result of the compressed axial magnetic field. It is possible that the LEH foil material mix in experiments is not confined to the axis in the way simulations predict. In this case, the maximum expected effect from the simulated mix can be calculated using the curves in Fig. 3, and assuming the peak simulated amount of the foil mix ( $0.9 \mu\text{g}$ ) is volumetrically mixed instantaneously at preheat into the fuel mass at stagnation ( $86.4 \mu\text{g}$ ). In this case, the percentage atomic mix of C-like atoms would be 0.13% and would degrade the yield by 40%. In reality, this is likely to be a very conservative estimate due to the assumptions made.

Compared to the with-DPP protocol, Fig. 13 shows almost no LEH foil mix for the co-injection protocol in the simulations. Differences in the way the co-injection protocol disassembles the LEH foil prevent significant LEH foil mass from entering the imploding region of the target. The dramatic difference in the LEH foil mix observed between the with-DPP and co-injection protocols broadly matches what was observed in experiments, as discussed in Sec. III A. This gives confidence that the simulations can effectively predict the relative axial transport of the LEH foil mix introduced by different preheat protocols. However, without additional data, we cannot say based on this analysis whether simulations predict the absolute amounts of the LEH foil mix, the radial distribution, or the impact of the mix on the performance accurately.

## V. CONCLUSIONS

Co and Mn coatings have been employed in integrated MagLIF shots to show the location where the material from various surfaces is present at stagnation by observing K shell emission lines from those coatings with an axially resolved spectrometer. The technique was employed on shots in which various preheat protocols were used. The results

suggest that laser preheat can push the LEH foil material into the imploding region of the targets. This was likely a source of material mixing in previously reported MagLIF experiments that used the no-DPP preheat protocol.<sup>2,3</sup> However, this analysis does not constrain the amount of LEH foil mix nor whether that mix had a significant impact on the target performance.

The LEH foil mix observed in the no-DPP and with-DPP preheat protocols helped motivate the design of a co-injection protocol guided by HYDRA simulations. The co-injection protocol used a low-energy pre-pulse early in time and a low-power foot pulse prior to a main pulse. In simulations, this significantly reduced the kinetic energy associated with the downwards-moving LEH foil material, and much less foil material was mixed into the imploding fuel. An integrated MagLIF experiment using the co-injection protocol showed no signature of the LEH foil mix, indicating that this source of mix had been effectively eliminated, as predicted by the simulations. This result gives us confidence that simulations can effectively design preheat protocols that minimize the LEH foil mix and also eliminates one potential performance degradation mechanism.

Co coatings were also applied to the top cushion region in some experiments. For the no-DPP preheat protocol, Co emission from the top cushion coating was observed only between 2 and 3.5 mm into the imploding region of the fuel, while for the with-DPP preheat protocol, Co emission was observed only between 4 and 6 mm into the fuel. In the with-DPP experiment, a 1-nm Mn coating was also placed on the fuel-facing side of the LEH foil. Mn appeared below the Co emission and remained relatively discrete at stagnation, suggesting that the top cushion material is being pushed in ahead of, and possibly by, the LEH foil material. Neutron yields produced in all experiments where a Co coating was applied to the top cushion suggest that only a small fraction of the coating is mixed into the imploding fuel region. However, the results do not constrain the amount of the Be mix generated from the top cushion.

While the coatings described in this paper can effectively show where axially the mix is present at stagnation in MagLIF, they cannot constrain the amount, timing, or the radial distribution of the mix introduced, all important quantities in determining the effect of the mix on integrated performance. Other techniques, such as a more advanced analysis of the spectra observed in these experiments at stagnation, may be able to constrain the amount of the mix present. It may also be possible in future experiments to apply a volumetric mid-Z dopant to the polyimide used in the LEH foils and to the Be used in the top and bottom cushions. This would allow the amount of the mix introduced from each of these target surfaces to be quantified. In particular, the use of Co-doped Be in the top and bottom cushions would allow the amount of this material mixed into the fuel to be assessed on each shot with little risk of further degrading the target performance and so assess whether the mix from these components is responsible for significant yield degradation. The time at which the mix is introduced into the fuel and the radial distribution of the mix material is harder to assess experimentally, and it may significantly affect the radiative losses and the impact that the mix has on stagnation.

## ACKNOWLEDGMENTS

The authors would like to thank the Z machine operations team, the ZBL operations team, the ABZ operations team, and the target fabrication team for their contributions to this work. We would also like to thank the Laboratory for Laser Energetics for help with designing the distributed phase plate optics used. Sandia National Laboratories is a multi-mission laboratory managed and operated by the National Technology and Engineering Solutions of Sandia, LLC., a wholly owned subsidiary of Honeywell International, Inc., for the U.S. Department of Energy's National Nuclear Security Administration under Contract No. DE-NA-0003525. This paper describes objective technical results and analysis. Any subjective views or opinions that might be expressed in this paper do not necessarily represent the views of the U.S. Department of Energy or the U.S. Government.

<sup>1</sup>S. A. Slutz, M. C. Herrmann, R. A. Vesey, A. B. Sefkow, D. B. Sinars, D. C. Rovang, K. J. Peterson, and M. E. Cuneo, *Phys. Plasmas* **17**, 056303 (2010).

<sup>2</sup>M. R. Gomez, S. A. Slutz, A. B. Sefkow, D. B. Sinars, K. D. Hahn, S. B. Hansen, E. C. Harding, P. F. Knapp, P. F. Schmit, C. A. Jennings, T. J.

Awe, M. Geissel, D. C. Rovang, G. A. Chandler, G. W. Cooper, M. E. Cuneo, A. J. Harvey-Thompson, M. C. Herrmann, M. H. Hess, O. Johns, D. C. Lamma, M. R. Martin, R. D. McBride, K. J. Peterson, J. L. Porter, G. K. Robertson, G. A. Rochau, C. L. Ruiz, M. E. Savage, I. C. Smith, W. A. Stygar, and R. A. Vesey, *Phys. Rev. Lett.* **113**, 155003 (2014).

<sup>3</sup>M. R. Gomez, S. A. Slutz, A. B. Sefkow, K. D. Hahn, S. B. Hansen, P. F. Knapp, P. F. Schmit, C. L. Ruiz, D. B. Sinars, E. C. Harding, C. A. Jennings, T. J. Awe, M. Geissel, D. C. Rovang, I. C. Smith, G. A. Chandler, G. W. Cooper, M. E. Cuneo, A. J. Harvey-Thompson, M. C. Herrmann, M. H. Hess, D. C. Lamma, M. R. Martin, R. D. McBride, K. J. Peterson, J. L. Porter, G. A. Rochau, M. E. Savage, D. G. Schroen, W. A. Stygar, and R. A. Vesey, *Phys. Plasmas* **22**, 056306 (2015).

<sup>4</sup>P. K. Rambo, I. C. Smith, J. L. Porter, M. J. Hurst, C. S. Speas, R. G. Adams, A. J. Garcia, E. Dawson, B. D. Thurston, C. Wakefield, J. W. Kellogg, M. J. Slattery, H. C. Ives, R. S. Broyles, J. A. Caird, A. C. Erlandson, J. E. Murray, W. C. Behrendt, N. D. Neilsen, and J. M. Narduzzi, *Appl. Opt.* **44**, 2421 (2005).

<sup>5</sup>S. A. Slutz, "Enhancing Performance of Magnetized Liner Inertial Fusion at the Z Facility," *Phys. Plasmas* (submitted).

<sup>6</sup>A. B. Sefkow, S. A. Slutz, J. M. Koning, M. M. Marinak, K. J. Peterson, D. B. Sinars, and R. A. Vesey, *Phys. Plasmas* **21**, 072711 (2014).

<sup>7</sup>S. B. Hansen, E. C. Harding, P. F. Knapp, M. R. Gomez, T. Nagayama, and J. E. Bailey, *Phys. Plasmas* **25**, 056301 (2018).

<sup>8</sup>E. C. Harding, T. Ao, J. E. Bailey, G. Loisel, D. B. Sinars, M. Geissel, G. A. Rochau, and I. C. Smith, *Rev. Sci. Instrum.* **86**, 043504 (2015).

<sup>9</sup>H. A. Scott and S. B. Hansen, *High Energy Density Phys.* **6**, 39 (2010).

<sup>10</sup>M. Geissel, T. J. Awe, D. E. Bliss, M. E. Campbell, M. R. Gomez, E. Harding, A. J. Harvey-Thompson, S. B. Hansen, C. Jennings, and M. W. Kimmel, and others, in *SPIE LASE* (International Society for Optics and Photonics, 2016), p. 973100–973100.

<sup>11</sup>M. Geissel, A. J. Harvey-Thompson, T. J. Awe, D. E. Bliss, M. E. Glinsky, M. R. Gomez, E. Harding, S. B. Hansen, C. Jennings, M. W. Kimmel, P. Knapp, S. M. Lewis, K. Peterson, M. Schollmeier, J. Schwarz, J. E. Shores, S. A. Slutz, D. B. Sinars, I. C. Smith, C. S. Speas, R. A. Vesey, M. R. Weis, and J. L. Porter, *Phys. Plasmas* **25**, 022706 (2018).

<sup>12</sup>S. A. Slutz, W. A. Stygar, M. R. Gomez, K. J. Peterson, A. B. Sefkow, D. B. Sinars, R. A. Vesey, E. M. Campbell, and R. Betti, *Phys. Plasmas* **23**, 022702 (2016).

<sup>13</sup>K. D. Hahn, G. W. Cooper, C. L. Ruiz, D. L. Fehl, G. A. Chandler, P. F. Knapp, R. J. Leeper, A. J. Nelson, R. M. Smelser, and J. A. Torres, *Rev. Sci. Instrum.* **85**, 043507 (2014).

<sup>14</sup>C. L. Ruiz, G. W. Cooper, S. A. Slutz, J. E. Bailey, G. A. Chandler, T. J. Nash, T. A. Mehlhorn, R. J. Leeper, D. Fehl, A. J. Nelson, J. Franklin, and L. Ziegler, *Phys. Rev. Lett.* **93**, 015001 (2004).

<sup>15</sup>S. B. Hansen, M. R. Gomez, A. B. Sefkow, S. A. Slutz, D. B. Sinars, K. D. Hahn, E. C. Harding, P. F. Knapp, P. F. Schmit, and T. J. Awe, *Phys. Plasmas* **22**, 056313 (2015).

<sup>16</sup>S. B. Hansen, E. C. Harding, P. F. Knapp, M. R. Gomez, T. Nagayama, and J. E. Bailey, *High Energy Density Phys.* **24**, 39 (2017).

<sup>17</sup>S. B. Hansen, private communication (2018).

<sup>18</sup>M. M. Marinak, G. D. Kerbel, N. A. Gentile, O. Jones, D. Munro, S. Pollaine, T. R. Dittrich, and S. W. Haan, *Phys. Plasmas* **8**, 2275 (2001).

<sup>19</sup>A. J. Harvey-Thompson, A. B. Sefkow, M. S. Wei, T. Nagayama, E. M. Campbell, B. E. Blue, R. F. Heeter, J. M. Koning, K. J. Peterson, and A. Schmitt, *Phys. Rev. E* **94**, 051201 (2016).